First ENA observations at Mars: Charge exchange ENAs produced in the magnetosheath

H. Gunell [a,b,*], K. Brinkfeldt [a], M. Holmström [a,1], P. C:son Brandt [c], S. Barabash [a], E. Kallio [d], A. Ekenbäck [a], Y. Futaana [a], R. Lundin [a], H. Andersson [a], M. Yamauchi [a], A. Grigoriev [a], J.D. Winningham [e], R.A. Frahm [e], J.R. Sharber [e], J.R. Scherrer [e], A.J. Coates [f], D.R. Linder [f], D.O. Kataria [f], T. Säles [d], P. Riihelä [d], W. Schmidt [d], H. Koskinen [g], J. Kozyra [h], J. Luhmann [i], E. Roelof [c], D. Williams [c], S. Livi [c], C.C. Curtis [j], K.C. Hsieh [j], B.R. Sandel [j], M. Grande [k], M. Carter [k], J.-A. Sauvaud [l], A. Fedorov [l], J.-J. Thocaven [l], S. McKenna-Lawler [b], S. Orsini [m], R. Cerulli-Irelli [m], M. Maggi [m], P. Wurz [n], P. Bochsler [n], N. Krupp [o], J. Woch [o], M. Fränz [o], K. Asamura [p], C. Dierker [q]

[a] Swedish Institute of Space Physics, Box 812, SE-981 28 Kiruna, Sweden
[b] Space Technology Ireland, National University of Ireland, Maynooth, Co. Kildare, Ireland
[c] Applied Physics Laboratory, Johns Hopkins University, Laurel, MD 20723-6099, USA
[d] Finnish Meteorological Institute, Box 503, FIN-00101 Helsinki, Finland
[e] Southwest Research Institute, San Antonio, TX 7228-0510, USA
[f] Mullard Space Science Laboratory, University College London, Surrey RH5 6NT, UK
[g] Department of Physical Sciences, University of Helsinki, P.O. Box 64, 00014 Helsinki
[h] Space Physics Research Laboratory, University of Michigan, Ann Arbor, MI 48109-2143, USA
[i] Space Science Laboratory, University of California at Berkeley, Berkeley, CA 94720-7450, USA
[j] University of Arizona, Tucson, AZ 85721, USA
[k] Rutherford Appleton Laboratory, Chilton, Didcot, Oxfordshire OX11 0QX, UK
[l] Centre d'Etude Spatiale des Rayonnements, BP-4346, F-31028 Toulouse, France
[m] Istituto di Fisica dello Spazio Interplanetari, I-00133 Rome, Italy
[n] Physikalisches Institut, University of Bern, CH-3012 Bern, Switzerland
[o] Max-Planck-Institut für Aeronomie, D-37191 Katlenburg-Lindau, Germany
[p] Institute of Space and Astronautical Science, 3-1-1 Yoshinodai, Sagamichara, Japan
[q] Technical University of Braunschweig, Hans-Sommer-Strasse 66, D-38106 Braunschweig, Germany

Abstract

Measurements of energetic neutral atoms (ENA) generated in the magnetosheath at Mars are reported. These ENAs are the result of charge exchange collisions between solar wind protons and neutral oxygen and hydrogen in the exosphere of Mars. The peak of the observed ENA flux is 1.3×10^{11} $m^{-2}\,sr^{-1}\,s^{-1}$. For the case studied here, i.e., the passage of Mars Express through the martian magnetosheath around 20:15 UT on 3 May 2004, the measurements agree with an analytical model of the ENA production at the planet. It is possible to find parameter values in the model such that the observed peak in the ENA count rate during the spacecraft passage through the magnetosheath is reproduced.
© 2005 Elsevier Inc. All rights reserved.

Keywords: Mars; Solar wind; Magnetospheres

---

* Corresponding author. Fax: +46 980 79050.
 E-mail address: herbert.gunell@physics.org (H. Gunell).

[1] Currently at NASA Goddard Space Flight Center, Laboratory for Solar and Space Physics, Mail Code 612.2, Greenbelt, MD 20771, USA.

1. Introduction

Energetic neutral atoms (ENAs) are produced by solar wind protons and newly created planetary ions that undergo charge exchange collisions with neutral atoms in the exospheres of the non-magnetised planets. For magnetised planets, like Earth, the exosphere is shielded from the solar wind by the magnetic field, and only plasma inside the magnetosphere can contribute to the ENA production. Charge exchange is one of the processes through which the solar wind interacts with planetary atmospheres. By measuring the ENA flux this interaction process can be studied. ENA measurements can also give information about the escape of pick-up ions since the charge exchange process that creates the ENAs also creates ions that can be picked up by the solar wind. ENA imaging is a powerful diagnostic tool to study the global distribution of single charge ions in planetary environments (Williams et al., 1992).

ENA images of Earth's magnetosphere have been obtained by the Swedish satellite Astrid (Brandt et al., 1999), by instruments on the IMAGE satellite (Burch et al., 2001), and on China's Double Star mission (McKenna-Lawlor et al., 2004). Holmström et al. (2002) simulated images of ENAs produced by the interaction between the solar wind and Mars through the integration of the ENA production along lines of sight to a virtual ENA instrument. Oxygen ENA images were considered by Barabash et al. (2002). Gunell et al. (2005a) compared the influence of different simulation models on the production and imaging of ENAs. Similar ENA simulations have also been performed for the Venus environment (Gunell et al., 2005b; Fok et al., 2004). ENAs play an important role in sputtering of the atmosphere, because as they are unaffected by electric and magnetic fields they move freely from high in the exosphere, where they are created in charge exchange collisions, to lower altitudes where they impact on the atmosphere and cause sputtering (Leblanc and Johnson, 2000).

In this work we present observations made with the Neutral Particle Imager (NPI) of the ASPERA-3 instrument on ESA's Mars Express mission (Barabash et al., 2004). For solar wind parameter estimates we also use the Ion Mass Analyser (IMA) and the Electron Spectrometer (ELS) of the ASPERA-3 instrument. The NPI measures energetic neutral atom fluxes in the vicinity of Mars. We compare our observations with simulations of ENAs that are based on a analytical model of the plasma flow around Mars (Kallio, 1996). This model has been used to study the role of charge exchange in Mars–solar wind interaction (Kallio et al., 1997), and was used by Holmström et al. (2002) to simulate ENA images. The computational technique used to calculate the ENA flux was described in detail by Holmström et al. (2002).

This paper is organised as follows. The observations are described in Section 2, the numerical simulations are presented in Section 3. In Section 4 the observational results are compared to the results from numerical simulations, and in Section 5 the conclusions are discussed.

2. Observations

The ASPERA-3 instrument consists of four sensors that measure electrons, ions and ENAs. In this work measurements made using the NPI sensor are analysed. We concentrate on data collected during Mars Express orbit 363 on 3 May 2004, when the spacecraft passed through the magnetosheath and into the solar wind. Fig. 1 shows the orbit in a cylindrical coordinate system, in which the x-axis is directed toward the Sun, the z-axis is directed northward, perpendicular to the ecliptic plane, and the y-axis closes the right-handed system. The distance to the Mars–Sun line is thus $\sqrt{y^2 + z^2}$. The bow shock and the induced magnetosphere boundary (IMB) are shown as dashed lines. The bow shock and IMB shapes shown in Fig. 1 are the same as those used for ENA calculations with the empirical model discussed in Section 3.

The IMB is the boundary which separates the solar wind from the inner region that is dominated by plasma of planetary origin. It has been given many different names in the literature depending on what measured quantity have been used to identify it. We call it the IMB following Lundin et al. (2004). The Sun is in the positive x-direction. Whether the IMB is the same boundary as the magnetic pile-up boundary (Vignes et al., 2000) cannot be determined by Mars Express that does not carry a magnetometer.

The NPI field of view is divided into 32 sectors, each with a $5° \times 11.25°$ field of view. Fig. 2 shows the position of Mars Express and the field of view of sectors 21–25 at 20:12:44 UT on 3 May 2004, when the spacecraft was in the magnetosheath. The grey-scale map shows a simulation of the ENA production rate in a plane that intersects the centre of all NPI sectors. The simulation is discussed further in Section 3. The ξ-axis is the projection of the Mars–Sun line in the NPI plane, and the ζ-axis is perpendicular to both the ξ-axis and the Mars–Sun line.
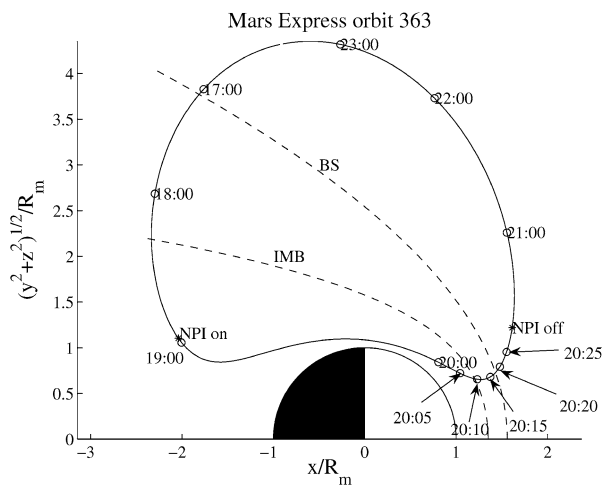
Fig. 1. Mars Express orbit 363 in cylindrical coordinates, with the bow shock (BS) and the induced magnetosphere boundary (IMB) shown. The bow shock and IMB shapes shown here are the same as those used for ENA calculations with the empirical model discussed in Section 3. The origin of the coordinate system is in the centre of Mars. The x-axis is directed toward the Sun, the z-axis is directed northward, perpendicular to the ecliptic plane, and the y-axis closes the right-handed system. $(y^2 + z^2)^{1/2}$ is the distance to the Mars–Sun line.

Fig. 3 shows the observed count rate for NPI sectors 21–25. A peak in the count rate is seen between 20:11 UT and 20:17 UT for sectors 22–24, and it can also be discerned in sectors 21 and 25, although it is less pronounced there. This peak is identified as ENAs originating in the main production region in the magnetosheath. The geometry can be seen in Fig. 2, which shows the spacecraft position at 20:12:44 and the field of view of the relevant sectors.
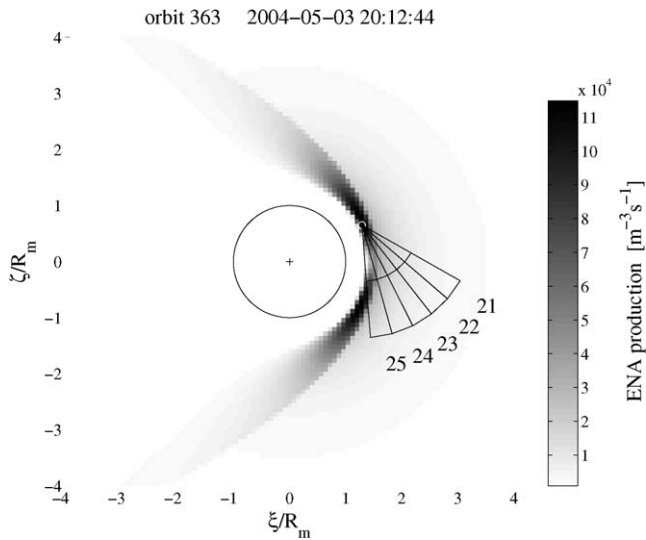
Fig. 2. Spacecraft position and field of view of sectors 21–25 at 20:12:44 UT on 3 May 2004. The grey-scale map shows a simulation of the ENA production rate in a plane that intersects the centre of all NPI sectors. The ξ-axis is the projection of the Mars–Sun line in the NPI plane, and the ζ-axis is perpendicular to both the ξ-axis and the Mars–Sun line.

There is another peak at about 19:50 UT followed by a slow decay that lasts until after the rise of the main peak described above when the spacecraft has entered the magnetosheath. This is most clearly seen in sectors 25 and 24, but traces are also seen in the other three sectors of Fig. 3. During the period from 19:50 to 20:10 the spacecraft was inside the IMB and the field of view covered the region between Mars and the IMB. The source of this signal could be ENAs or a contamination by ultraviolet light reflected from the surface or scattered in the atmosphere. A simple UV model is used to study this issue in Section 3.

3. Simulations

An empirical model for the plasma flow around Mars based on measurements made with the ASPERA (Automatic Space Plasma Experiment with a Rotating Analyser) instrument on board the Phobos 2 spacecraft was developed by Kallio (1996). This model was used to study the production of energetic neutral atoms through charge exchange collisions between the solar wind protons and atoms and molecules in the martian neutral atmosphere (Kallio et al., 1997). It has also been used to study the motion of protons and oxygen ions near Mars (Kallio and Koskinen, 1999). The model is cylindrically symmetric with respect to the Mars–Sun axis, and includes a bow shock and an induced magnetosphere boundary. The magnetic field is frozen into the modelled flow. A spherical obstacle, that is impenetrable to the flow, is assumed at 170 km altitude. The bow shock shape is given by a conical function that is based on Mariner 4, Mars 2, 3, 5, and Phobos 2 bow shock crossings. The shape of the induced magnetosphere boundary is given by an even fourth-order polynomial based on Phobos 2 data. The model is
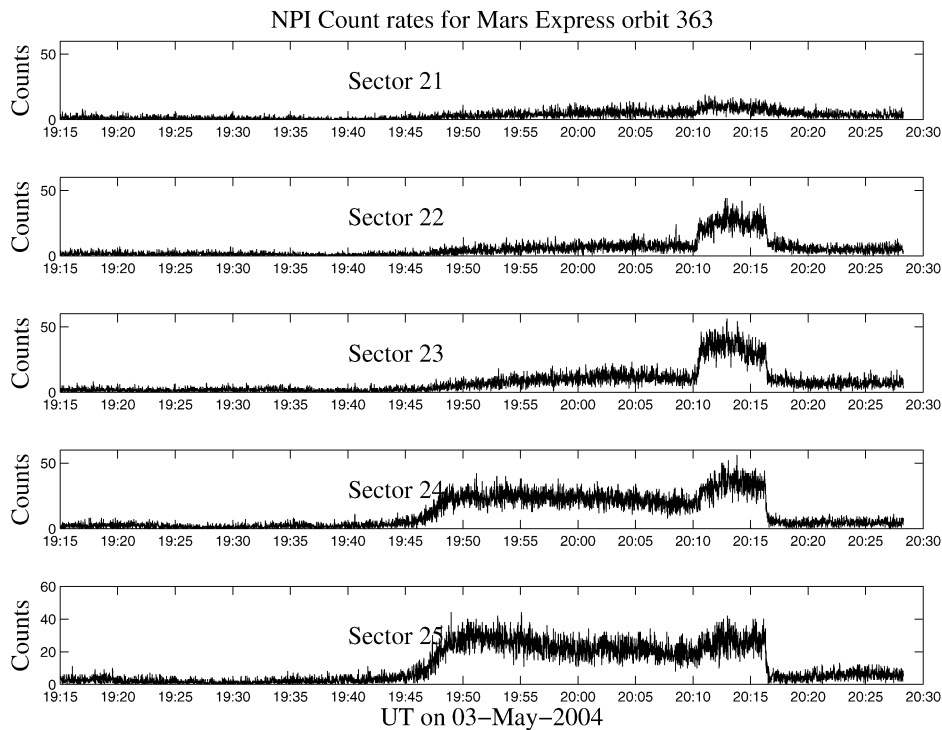
Fig. 3. Orbit 363 data from the ASPERA-3 NPI sensor.

Table 1
Model parameters used by Holmström et al. (2002) compared to the parameters used here (the model obstacle is located at 170 km altitude)

Parameter	Holmström	This work
Solar wind		
Plasma density	2.5×10^6 m^{-3}	2.0×10^6 m^{-3}
Temperature	10 eV	5 eV
Solar wind speed	400 km s^{-1}	470 km s^{-1}
Geometry		
Bow shock position	1.55 R_m	1.55 R_m
IMB position	1.2 R_m	1.35 R_m
IMB penetration	1/6	0.05
Neutral exobase		
H density	9.9×10^{11} m^{-3}	2.97×10^{12} m^{-3}
H temperature	192 K	192 K
H$_2$ density	3.8×10^{12} m^{-3}	1.14×10^{13} m^{-3}
H$_2$ temperature	192 K	192 K
O$_{\text{hot}}$ density	5.5×10^9 m^{-3}	1.65×10^{10} m^{-3}
O$_{\text{hot}}$ temperature	4.4×10^3 K	4.4×10^3 K
O$_{\text{thermal}}$ density	1.4×10^{14} m^{-3}	4.2×10^{14} m^{-3}
O$_{\text{thermal}}$ temperature	173 K	173 K

parameterised, and the parameter values used here are shown in Table 1, that also shows the parameters used by Holmström et al. (2002), for comparison.

The algorithm for computing ENA images was described in detail by Holmström et al. (2002). The ENA production in the direction from the source toward the instrument is integrated along lines of sight from the position of the NPI on the spacecraft. The production rate is proportional to the density of the neutral exosphere, the directional proton flux, and the cross sections for charge exchange with the different neutral species. We use the model for the cross sections that was used by Kallio et al. (1997). The proton velocity distribution is assumed to be a Maxwellian that is centred around the bulk velocity given by the empirical plasma flow model. The simulated count rates shown in Fig. 4 have been computed by weighted average of 434 line of sight integrals for each sector. The weights are given by the sensitivity of the NPI for ENAs incident from different directions. The various directions were scanned during calibrations yielding a 14×31 matrix for the directional sensitivity.

When calculating the ENA flux a Chamberlain exosphere is used to model the neutral gas density. The number density n_i of neutral species i is modelled as $n_i = N_i \exp(-\beta_i(1/r_0 - 1/r))\zeta(\beta_i/r)$, where r is the distance to the centre of Mars, r_0 is the radius of the exobase, ζ is Chamberlain's partition function (Chamberlain and Hunten, 1987), and β_i is a constant that is determined by the mass and temperature of each species. $\beta_i = GMm_i/(k_B T_i)$, where G is the gravitational constant, $M = 6.46 \times 10^{23}$ kg is the mass of Mars, m_i is the atomic mass of neutral species i, and T_i is the temperature of species i at the exobase. The exobase altitude is assumed to coincide with the model obstacle at 170 km. The properties of the exosphere are variable and the true conditions for the day of the observation unknown. Therefore the parameters of the density profiles shall be seen as a an analytical fit rather than a true set of parameters for the exosphere on the day of the observation. The exosphere parameters are varied in Section 4 to fit the

model results to the observations. Three species are included in the model: atomic hydrogen, molecular hydrogen, and oxygen. For oxygen two populations with different temperatures are modelled.

We started with exosphere parameters that were adopted from Kallio et al. (1997), Holmström et al. (2002), Krasnopolsky and Gladstone (1996), and then the geometrical and exospheric parameters were varied to fit the observed data. The solar wind parameters were estimated from IMA and ELS data and kept fixed at these estimated values. The parameters are shown in Table 1, the initial parameters being found in the column labelled Holmström. The quantity called "IMB position" in Table 1 is defined as the planetocentric distance to the point where the induced magnetosphere boundary intersects the Mars–Sun line. It was varied to obtain a good agreement with the rising edge of the main peak in the count rate for sector 23. This is achieved with an IMB position of 1.35 R_m. To fit the peak count rate the density at the model obstacle was also increased by a factor of three. This increases the neutral density everywhere and hence increases the ENA production. The IMB penetration parameter was decreased from 1/6 to 0.05. This changes the stream lines and increases the proton flux in the magnetosheath thus contributing to a higher ENA flux at the observed peak. A careful study of the influence of the different parameters on the ENA flux as well as on the shape and structure of ENA images was published by Holmström et al. (2002). The modelling result is shown in Fig. 4. The bow shock and the IMB are shown in Fig. 1 using these parameters. The spacecraft crosses the induced magnetosphere boundary at 20:10 in this model, and the bow shock is crossed at 20:18. This means that the main peak of the ENA flux started shortly after the spacecraft entered the magnetosheath and ended a minute before the spacecraft crossed the bow shock and entered the solar wind.

We have made a simplified simulation of ultraviolet light from Lyman alpha airglow to investigate the possible contamination of the data by UV photons. The model is based on Bush and Chakrabarti (1995b), but is simplified by assuming only single scattering of the incident sunlight. The count rate R_{UV} caused by UV photons is estimated by a line of sight integral

$$R_{\text{UV}} = A\sigma Q \frac{\Omega}{4\pi} \int_{\text{LOS}} S_{\text{sun}} e^{-\tau(s)} \, ds, \tag{1}$$

where τ is the optical depth along the line of sight:

$$\tau(s) = \sigma \int_0^s n_{\text{H}}(s') \, ds' \tag{2}$$

and $A = 5.25 \times 10^{-5}$ m^2 is the detector area, $\sigma = 1.19 \times 10^{-17} \times \sqrt{T_0/T_{\text{H}}}$ m^2 is the photo absorption cross section (Bush and Chakrabarti, 1995b), where $T_0 = 1000$ K. $Q = 5 \times 10^{-6}$ is the quantum efficiency of the NPI, Ω the solid angle of the field of view, and n_{H} is the density of neutral hydrogen in the exosphere. The source function S_{sun} is given by

$$S_{\text{sun}}(x, y, z) = \phi_s \int_x^{x_0} e^{-\tau(x', y, z)} \, dx', \tag{3}$$

NPI Count rates for Mars Express orbit 363
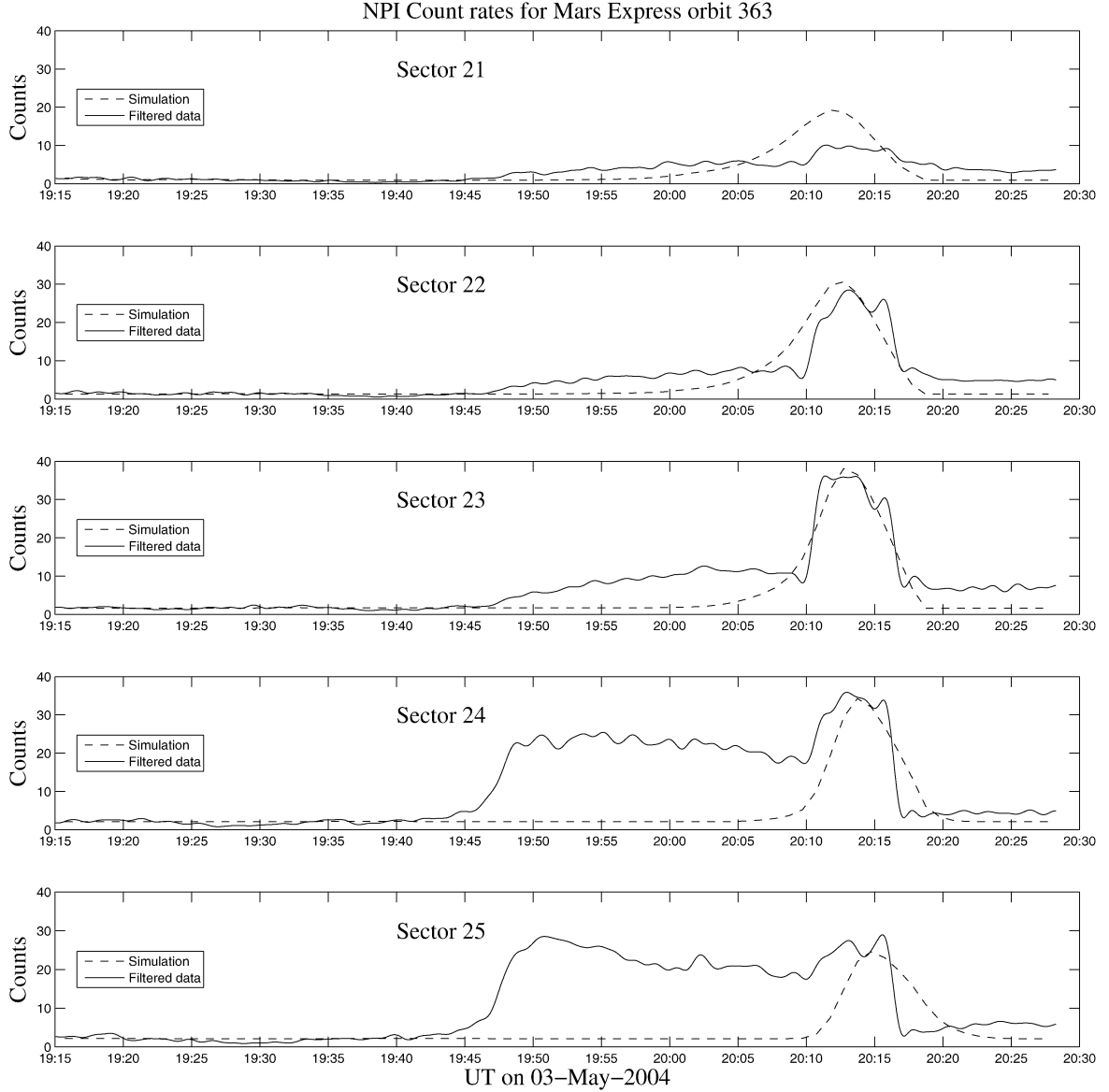
Fig. 4. Simulations (dashed curves) and filtered data (solid curves) from MEX orbit 363 and the ASPERA-3 NPI sensor. The highest count rates in sectors 23 and 24 correspond to fluxes of 1.3×10^{11} and 1.2×10^{11} m^{-2} sr^{-1} s^{-1}, respectively. The dark counts shown in Table 2 have been added to the simulation results.

where $x_0 = 20$ R_{m} is the sunward edge of the simulation region, ϕ_{s} is the incident Lyman alpha flux within the Doppler bandwidth. The value for the solar Lyman alpha is obtained from the Solar2000 model (Tobiska et al., 2000) and is scaled by the square ratio of the Earth–Sun and Mars–Sun distances and the Doppler bandwidth to solar emission line bandwidth ratio. The Lyman alpha line that is emitted from the sun is 0.9 Å wide, whereas photons can only be absorbed within the more narrow Doppler bandwidth of the martian exosphere (Bush and Chakrabarti, 1995a). Thus the incident flux is

$$\phi_{\mathrm{s}} = 3.99 \times 10^{15} \times (1.008/1.621)^2 \times (0.0164/0.9) \ \mathrm{m}^{-2}\,\mathrm{s}^{-1}$$

$$= 2.81 \times 10^{13} \ \mathrm{m}^{-2}\,\mathrm{s}^{-1}.$$

Finally $\tau(x, y, z)$ in Eq. (3) is defined by

$$\tau(x, y, z) = \sigma \int_{x}^{x_0} n_{\mathrm{H}}(x', y, z) \, \mathrm{d}x', \tag{4}$$

where the path of integration is parallel with the x-axis and runs from the source point in question to $x = x_0$.

Analogously to the ENA simulations described above a weighted average is then formed using the measured relative sensitivities for different angles of incidence. The quantum efficiency and the relative directional sensitivities were obtained in calibrations of the NPI reference model. This introduces an uncertainty of the absolute count rate, but the simulation result can still serve as a relative measure of the contribution from ultraviolet light, and the shape of the curves shown in Fig. 5 can be compared to the shape of the curves showing observed count rate in Fig. 3.
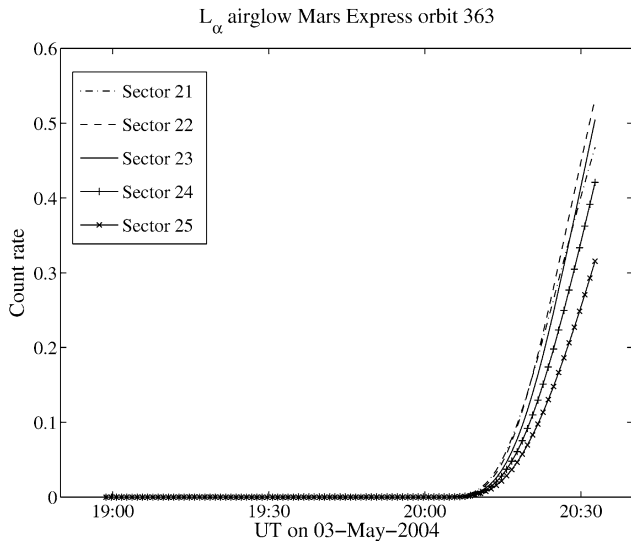
Fig. 5. A simulation of the count rate caused by Lyman alpha airglow from the martian hydrogen corona.

Table 2
ENA flux observed by the ASPERA-3 NPI and the dark count and sensitivity that was used to calculate the flux

Sector	Flux ($m^{-2}\,sr^{-1}\,s^{-1}$)	Dark count	Sensitivity ($m^{-2}\,sr^{-1}$)
21	3.4×10^{10}	0.9	5.2×10^{-10}
22	1.0×10^{11}	1.3	6.8×10^{-10}
23	1.3×10^{11}	1.6	7.9×10^{-10}
24	1.2×10^{11}	2.1	8.0×10^{-10}
25	9.9×10^{10}	2.1	7.9×10^{-10}

4. Results

Fig. 4 shows the data of Fig. 3, which has been digitally filtered to remove high frequency noise. The filter is a low-pass finite impulse response filter of length 201, with real and symmetric coefficients. The signal is run first forward and then backward through the filter, thus obtaining precisely zero phase distortion. Signals with a period less than one minute are attenuated efficaciously. The dashed lines show the result of the simulation described in Section 3. Using this filtered data we calculate the maximum ENA flux for each sector, during the main peak between 20:11 and 20:17 UT. The result is shown in Table 2. The flux is computed by subtracting the dark count from each sector and multiplying by the sensitivity, that is to say

$$j_{ENA} = \frac{R - R_{dark}}{G\epsilon}, \tag{5}$$

where j_{ENA} is the ENA flux, R is the observed count rate, R_{dark} is the dark count, $G = 2.7 \times 10^{-7}$ m^2 sr is the geometrical factor, and ϵ is the efficiency for each sector. The sensitivity that is tabulated in Table 2, along with the flux and the dark count, is then defined as $1/(G\epsilon)$. Since the NPI does not resolve particle energy the efficiency corresponding to 1 keV was used. The dark count is estimated as the mean of the count rate between the times 19:15 and 19:45. The maximum value

in sector 23 is 1.3×10^{11} $m^{-2}\,sr^{-1}\,s^{-1}$ which is in agreement with the highest emission from the shocked solar wind predicted by Holmström et al. (2002), as shown in Plate 1 of that paper.

There are a few uncertainties that can contribute to an error in the flux that is calculated from the data. First, there can be an error in the calibrated sensitivity. This error is less than 25%. Secondly, the sensitivity depends on the incident angle within each sector, and since we cannot know the exact incident angle we have used the sensitivity for the central direction of each sector, where the sensitivity is at its peak. Thirdly, the efficiency depends on the particle energy, and since we do not know the energy of the incident ENAs this can contribute to an error in the measured flux. For typical solar wind energies, i.e., $E = 1$ keV for hydrogen, where $\epsilon = 10^{-3}$, this error is approximately

$$\frac{\Delta\epsilon}{\Delta E} = 7.4 \times 10^{-4} \text{ (eV}^{-1}).$$

The result of the UV simulation, which is shown in Fig. 5, is that the maximum count rate is approximately 0.5 s^{-1}, i.e., lower than the observed count rate by a factor of 10–100. The shape of the simulated UV curves is completely different from that of the observed count rates (Figs. 3 and 4) and thus even if the quantum efficiency of the instrument was off by a very large factor the observed peak between 20:11 and 20:17 cannot be caused by this UV source.

5. Conclusions and discussion

We have presented data from the Neutral particle imager of the ASPERA-3 instrument on ESA's Mars Express mission. During orbit 363 between 20:11 and 20:17 UT on 3 May 2004 a peak appeared in the observed count rate. It both rises and falls off very sharply. The maximum flux is approximately 10^{11} $m^{-2}\,sr^{-1}\,s^{-1}$ in agreement with the predictions by Holmström et al. (2002). The source of the observed flux is ENAs created in charge exchange collisions between atoms in the atmosphere of Mars and solar wind protons. The source region is located in the shocked solar wind between the bow shock and the induced magnetosphere boundary. The field of view is shown in Fig. 2 on a map of the ENA production rate. The ENAs that can reach the instrument are created between the spacecraft and the Mars–Sun line, because the ENA flux is highly directional and parallel with the plasma velocity at the source point. The bulk velocity of the plasma downstream of the bow shock is directed diagonally outward from the Mars–Sun line.

The model parameter that is the most influential on the morphology of ENA images is the IMB position (Holmström et al., 2002). The IMB position is in turn likely to be influenced by the solar wind parameters. Combining ENA measurements with solar wind measurements can be a useful technique for future studies of this dependence. The data agrees with simulations using an IMB position, defined as the planetocentric distance to the IMB along the Mars–Sun line, of 1.35 R_m, and an, analogously defined, bow shock position of 1.55 R_m. This estimate

of the parameters relies on the assumption that these boundaries were shaped according to the model we used. These boundaries are known to be variable. The increase of the ENA flux that is seen in the simulation is not as sharp as the increase of the measured signal. The model is based on a statistical study of several orbits and is therefore an average rather than a momentary picture of the IMB. This introduces an uncertainty into the identification of the IMB position at 1.35 R_m. Combined studies of ENA data and measurements of other quantities provide a promising way to study the shape of these boundaries. While measurements of electrons and ions are local ENA measurements are non-local, and thus in effect one spacecraft can provide simultaneous measurements over an extended region.

The exosphere parameters were varied to achieve better agreement for the value of the count rate at the main peak. The set of parameters arrived at in this way is not a unique solution. The properties of the exosphere vary with time, and the exact conditions for the day of the observation are unknown. We merely fit a function to the observed data, and do not claim that the actual exosphere had the parameters that we arrived at. The necessary increase of the exosphere density in the ENA production region could be accomplished through other exobase altitudes, densities, and temperatures. At the altitudes that are considered here the oxygen component of the exosphere, although it has been included in the models, is negligible in comparison with the hydrogen component. One application of ENA measurements is parameter extraction by Holmström and Kallio (2004). Future work may improve our abilities to extract parameters from these ENA measurements.

The peak at 19:50 and the following slowly decreasing plateau seen in some of the sections could either be caused by ENAs scattered off the atmosphere or possibly by contamination of the data by ultraviolet photons. Ultraviolet light reflected from the surface could have reached sector 25 at 19:50 as the field of view of that sector just about touched the martian surface at that time, but the sustained plateau cannot be explained in this way. A simulation of Lyman alpha emissions from the atmosphere yields a count rate that is lower than the observed count rate by a factor of 10–100. There is some uncertainty in this, since the calibrations were performed on the reference model rather than on the instrument itself. Further increasing the uncertainties the UV model depends on the density profile of the exosphere, of which detailed knowledge is unavailable at this time. The shape of the curves of the UV emissions, however, excludes UV as a source for the main peak between 20:11 and 20:17 UT.

This study shows that the general picture of the generation of ENAs at Mars is correct. ENAs are generated in the between the bow shock and the induced magnetosphere boundary, and the flux agrees with predicted values. Now that a general agreement has been confirmed ENA measurements can be used in future work for automated parameter extraction; to study mass loading, the shape and variability of plasma boundaries; and for comparison between different Mars–solar wind interaction models.

References

Barabash, S., Holmström, M., Lukyanov, A., Kallio, E., 2002. Energetic neutral atoms at Mars. IV. Imaging of planetary oxygen. J. Geophys. Res. 107 (A10), doi:10.1029/2001JA000326. 1280.

Barabash, S., and 46 colleagues, 2004. ASPERA-3: Analyser of space plasmas and energetic ions for Mars Express. In: Wilson, A. (Ed.), Mars Express: The Scientific Payload, ESA SP-1240. European Space Research and Technology Centre, Noordwijk, The Netherlands, pp. 121–139.

Brandt C:son, P., Barabash, S., Norberg, O., Lundin, R., 1999. Energetic neutral atom imaging at low altitudes from the Swedish microsatellite Astrid: Images and spectral analysis. J. Geophys. Res. 104 (A2), 2367–2379.

Burch, J.L., Mende, S.B., Mitchell, D.G., Moore, T.E., Pollock, C.J., Reinisch, B.W., Sandel, B.R., Fuselier, S.A., Gallagher, D.L., Green, J.L., Perez, J.D., Reiff, P.H., 2001. Views of Earth's magnetosphere with the IMAGE satellite. Science 291 (5504), 619–624.

Bush, B.C., Chakrabarti, S., 1995a. Analysis of Lyman α and He I 584-Å airglow measurements using a spherical radiative transfer model. J. Geophys. Res. 100 (A10), 19609–19625.

Bush, B.C., Chakrabarti, S., 1995b. A radiative transfer model using spherical geometry and partial frequency redistribution. J. Geophys. Res. 100 (A10), 19627–19642.

Chamberlain, J.W., Hunten, D.M., 1987. Theory of Planetary Atmospheres, second ed. Academic Press, San Diego, CA.

Fok, M.-C., Moore, T.E., Collier, M.R., Tanaka, T., 2004. Neutral atom imaging of solar wind interaction with the Earth and Venus. J. Geophys. Res. 109 (A1), doi:10.1029/2003JA010094. A01206.

Gunell, H., Holmström, M., Barabash, S., Kallio, E., Janhunen, P., Nagy, A.F., Ma, Y., 2005a. Planetary ENA imaging: Effects of different interaction models for Mars. Planet. Space Sci. doi:10.1016/j.pss.2005.04.002. In press.

Gunell, H., Holmström, M., Biernat, H.K., Erkaev, N.V., 2005b. Planetary ENA imaging: Venus and a comparison with Mars. Planet. Space Sci. 53 (4), 433–441, doi:10.1016/j.pss.2004.07.021.

Holmström, M., Kallio, E., 2004. The solar wind interaction with Venus and Mars: Energetic neutral atom and X-ray imaging. Adv. Space Res. 33 (2), 187–193.

Holmström, M., Barabash, S., Kallio, E., 2002. Energetic neutral atoms at Mars. I. Imaging of solar wind protons. J. Geophys. Res. 107 (A10), doi:10.1029/2001JA000325. 1277.

Kallio, E., 1996. An empirical model of the solar wind flow around Mars. J. Geophys. Res. 101, 11133–11147.

Kallio, E., Koskinen, H., 1999. A test particle simulation of the motion of oxygen ions and solar wind protons near Mars. J. Geophys. Res. 104, 557–579.

Kallio, E., Luhmann, J.G., Barabash, S., 1997. Charge exchange near Mars: The solar wind absorption and energetic neutral atom production. J. Geophys. Res. 102, 22183–22197.

Krasnopolsky, V.A., Gladstone, G.R., 1996. Helium on Mars: EUVE and PHO-BOS data and implications for Mars' evolution. J. Geophys. Res. 101 (A7), 15765–15772.

Leblanc, F., Johnson, R.E., 2000. Sputtering of the martian atmosphere by solar wind pick-up ions. Planet. Space Sci. 49, 645–656.

Lundin, R., and 44 colleagues, 2004. Solar wind-induced atmospheric erosion at Mars: First results from ASPERA-3 on Mars Express. Science 305, 1933–1936.

McKenna-Lawlor, S., and 13 colleagues, 2004. The energetic NeUtral Atom Detector Unit (NUADU) for China's Double Star mission and its calibration. Nucl. Instrum. Methods Phys. Res. A 530, 311–322.

Tobiska, W.K., Woods, T., Eparvier, F., Viereck, R., Floyd, L., Bouwer , D., Rottman, G., White, O.R., 2000. The SOLAR2000 empirical solar irradiance model and forecast tool. J. Atmos. Terr. Phys. 62, 1233–1250.

Vignes, D., Mazelle, C., Rme, H., Acuña, M.H., Connerney, J.E.P., Lin, R.P., Mitchell, D.L., Cloutier, P., Crider, D.H., Ness, N.F., 2000. The solar wind interaction with Mars: Locations and shapes of the bow shock and the magnetic pile-up boundary from the observations of the MAG/ER experiment onboard Mars Global Surveyor. Geophys. Res. Lett. 27 (1), 49–52.

Williams, D.J., Roelof, E.C., Mitchell, D.G., 1992. Global magnetospheric imaging. Rev. Geophys. 30, 183–208.